# Quantifying assays: inhibition of signalling pathways of cancer

Roumen Anguelov[*]

*Department of Mathematics and Applied Mathematics, University of Pretoria, Private Bag X20,
Hatfield 0028, South Africa*
*Institute of Mathematics and Informatics, Bulgarian Academy of Sciences, Acad. Georgi Bonchev St.,
Block 8, Sofia 1113, Bulgaria*
[*]Corresponding author. Email: roumen.anguelov@up.ac.za

G. Manjunath and Avulundiah E. Phiri

*Department of Mathematics and Applied Mathematics, University of Pretoria, Private Bag X20,
Hatfield 0028, South Africa*

Trevor T. Nyakudya and Priyesh Bipath

*Department of Physiology, University of Pretoria, Private Bag X20, Hatfield 0028, South Africa*

June C. Serem

*Department of Anatomy, University of Pretoria, Private Bag X20, Hatfield 0028, South Africa*

and

Yvette N. Hlophe

*Department of Physiology, University of Pretoria, Private Bag X20, Hatfield 0028, South Africa*

Inhibiting a signalling pathway concerns controlling the cellular processes of a cancer cell's viability, cell division and death. Assay protocols created to see if the molecular structures of the drugs being tested have the desired inhibition qualities often show great variability across experiments, and it is imperative to diminish the effects of such variability while inferences are drawn. In this paper, we propose the study of experimental data through the lenses of a mathematical model depicting the inhibition mechanism and the activation-inhibition dynamics. The method is exemplified through assay data obtained from an experimental study of the inhibition of the chemokine receptor 4 (CXCR4) and chemokine ligand 12 (CXCL12) signalling pathway of melanoma cells. The quantitative analysis is conducted as a two step process: (i) deriving theoretically from the model the cell viability as a function of time depending on several parameters; (ii) estimating the values of the parameters by using the experimental data. The cell viability is obtained as a function of concentration of the inhibitor and time, thus providing a comprehensive characterization of the potential therapeutic effect of the considered inhibitor, e.g. $IC_{50}$ can be computed for any time point.

*Keywords*: cancer assay; cell-viability; experimental variability; dynamical modeling.

## 1. Introduction

Cell signaling is essential for the functioning and survival of individual cells and biological organisms. Understanding the signaling pathways presents an opportunity to get insight into the mechanism of the disease and design therapeutic interventions. The review papers by Aldridge *et al.* (2006) and

Hendriks (2010), which make this point, further discuss the role mathematical modelling can play in describing and analysing regulatory networks as well as identifying therapeutic interventions via activation or inhibition of specific pathways.

Cancer, being the leading cause of mortality in the world (Sung *et al.*, 2021), attracts a significant research effort, including in its forefront research employing mathematical models for feasibility and quantitative analysis over wide spectrum of cancers and treatment procedures, e.g. Lima *et al.* (2016), Jenner *et al.* (2020), Bonilla *et al.* (2021), Cardinal *et al.* (2022), Ruiz-Martinez *et al.* (2022). A general model of control/inhibition of signalling pathways is introduced in Lee *et al.* (2021) with application to a study of how an intracellular signalling network comprising signal transducers and activators of transcription (STAT), B-cell lymphoma 2 (BCl2) and Bcl-2-associated X protein (BAX) regulates important cellular states, either anti-apoptosis or apoptosis of cancer cells. The recent paper by Chang *et al.* (2022) determines combination treatment of two tyrosine kinase inhibitors to treat disrupted intracellular calcium signalling in oesophageal cancer. A mathematical simulation model was used to determine the ratio of the inhibitors to produce a synergistic response. A mathematical model on melanoma cancer using kinase inhibitors in combination with inhibitors of barrier proteins is discussed by Nave & Sigron (2022).

The focus of this work is on suppression of the cell viability of melanoma via blocking the CXCR4 receptors on the cell membranes. CXCR4 is a receptor for the ligand CXCL12. The CXCL12/CXCR4 axis activates signal pathways promoting cell proliferation and migration. Its prominent role in many cancers is well studied in general, e.g. Wong & Korz (2008); Chatterjee *et al.* (2014), as well as for specific cancers, Cardones *et al.* (2003); Orimo *et al.* (2005); Biascia *et al.* (2020).

We propose a mathematical model representing the dynamics of activation and inhibition of the CXCL12/CXCR4 axis. In the established terminology (Hendriks, 2010), this is a kinetic model, mathematically represented as a system of differential equations. Inhibition is usually modelled by setting the growth rate to be a generic, i.e. not process-specific, decreasing function of the inhibitor (Lee *et al.*, 2021). We propose an alternative approach, which takes into account the specific biological mechanism effecting the inhibition of the CXCL12/CXCR4 axis. More precisely, we model the interplay of activation and inhibition of this axis as a competitive dynamical system.

A well-recognized challenge of applications of kinetic models of signalling pathways is the large number of parameters involved and the practical difficulty to identify their values in a unique way from the available data (Aldridge *et al.*, 2006). Although the competitive system representing the activation-inhibition dynamics is relatively simple and can be reduced to a system of two differential equations, the challenge of large number of parameters is well pronounced. Rather than trying to identify the model parameters, we derive theoretically the variable of interest, namely the cell viability. This new approach to kinetic models reduces significantly the number of parameters and provides an efficient way for integrating them with experimental data. In the specific setting under consideration, mathematical analysis of the model as a dynamical system yields an approximate representation of the cell-viability as a function of time depending on four parameters. Further numerical and data analysis reduces the number of parameters to two. These were estimated from the data in a very robust way.

Cell viability data were obtained at several time points and under varied concentration of the inhibitor using the crystal violet assay (Feoktistova *et al.*, 2016). As with all experiments, crystal violet assay has advantages and limitations (Larramendy & Soloneski, 2018, Chapter 1), certain measurement error can be expected. There may be yet another fundamental source for data variability. One crucial aspect of the test is that once a group of cells has undergone the crystal violet assay, another measurement of a cell population cannot be made at a future time since a measurement causes the cell to be in a fixed

(non-metabolizing) condition that prevents further growth. Therefore, every data point is a measurement of a different group of cells. This suggests that, even though the cells are maintained properly, and used their healthiest growth phase, the data's variability also likely reflects the variations in the properties of the cell groups and their initial states in the different wells. Hence, the observed variability of experimental data is not unexpected. Fitting a theoretically derived type of functions to the experimental data limits the effects of variability in the sense that (i) the type of function is predefined and not affected by the observed data; (ii) data trends inconsistent with the function type (e.g. cell viability increasing with time or inhibitor concentration) are eliminated; (iii) estimating a small number of parameters is less dependant on variations of the data. Hence, one can reasonably expect that the results obtained here regarding cell viability are more robust (getting a similar outcome should the experiment be repeated) compared to purely data-based analysis like approximation/curve fitting and/or statistics. For example, approximations of the data are highly dependent on the chosen type of functions and optimization criterion, e.g. Khinkis *et al.* (2003). Further, the estimated values of the parameters are not necessarily endowed with a biological meaning. Haibe-Kains *et al.* show in Haibe-Kains *et al.* (2013) that statistics only based study of measurements in cell inhibitory assays may lead to inconsistent results for the same drug across assays.

The proposed integration of data with existing biological knowledge embedded in a model provides for, on the one hand, reliably (in the sense discussed above) establishing time dynamics of interest and, on the other hand, a better understanding of the biological processes by more detailed interpretation of the data, e.g. identifying the main drivers of the observed dynamics.

The remainder of this paper is organized as follows. In Section 2, we introduce a mathematical model to capture the inhibition dynamics and the resultant effect on the cell viability. The model is derived as a system of ordinary differential equations and analysed as a dynamical system. To facilitate a first reading of the paper, the technical proof of the main theorem is moved to the Appendix. The conducted experiments under the crystal violet assay protocol using L-Kynurenine as an inhibiting agent are described in Section 3. The graphical representation of the data demonstrates both the variability of data and the existence of a trend. Using the mathematical model, we construct in Section 4 the theoretical cell viability variable in a specific form as a function of time depending on several parameters. Section 5 deals with fitting the theoretical cell viability to the set of data as well as some interpretation of the obtained results. Application to deriving $IC_{50}$ for all times within the time range of the experiments is presented in Section 6. It is further shown that the method can produce the inhibiting concentration as functions of time for any other level of cell viability, e.g. 30% or 70%. Concluding remarks and some questions are discussed in the last section.

## 2. Model development and its mathematical analysis

Since more cancer cells are expected to die in the presence of an inhibiting drug, the amount of inhibition in the micro-environment of a cancer cell would also be expected to vary with time. We introduce a mechanistic model that deals with the inhabitancy of the inhibiting molecules on the cancer cell. Melanoma cells express chemokine receptor 4 (CXCR-4) located on the cell membrane (Wong & Korz, 2008). When the chemokine ligand 12 (CXCL12) bounds to CXCR4, it activates signalling pathways such as mitogen-activated protein kinase (MAPK) and phosphatidylinositol 3-kinase (PI3K). The activated signaling pathways promote cancer cell proliferation, migration and adhesion. Hence, the CXCL12/CXCR-4 axis is crucial in cancer metastasis.

The investigation, both qualitatively and quantitatively, of the temporal dynamics of blocking this axis, is the focus of this section, see Fig. 1.
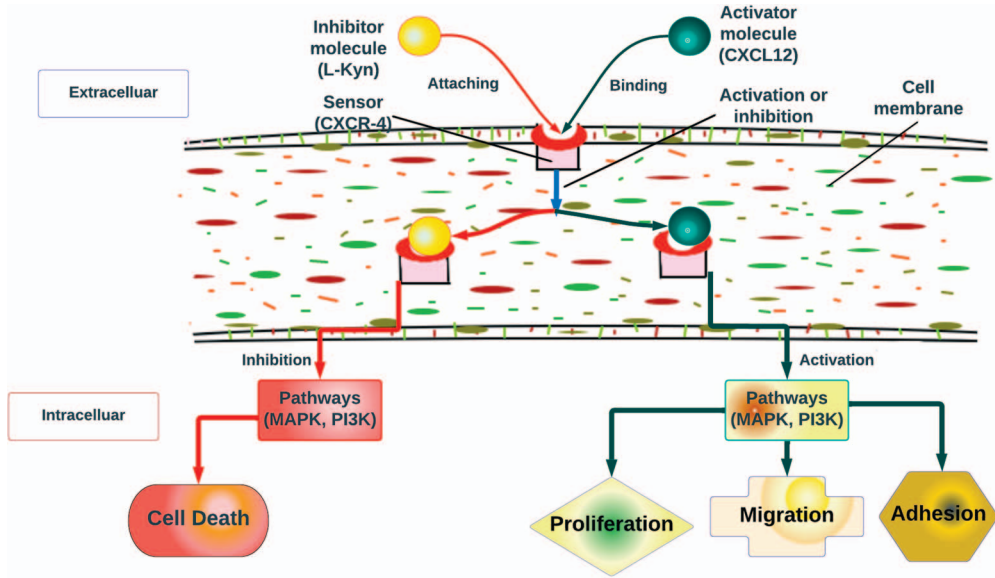
FIG. 1. Signaling pathways are activated when the activator molecule, chemokine ligand 12 (CXCL12), connects to the chemokine receptor 4 (CXCR4). Cell migration, adhesion and proliferation follow from this. Inhibition of signaling pathways occurs when a molecule of the inhibitor, L-Kynurenine (L-Kyn), binds to the sensor CXCR4. As a result, the cell's regular functioning is adversely impacted, which causes cell death.

## 2.1  *Mathematical model*

Depending on which agent, the activator CXCL12 or an inhibitor docks on the sensor CXCR4 at each time instant, the signaling pathway for producing essential for the survival and proliferation of the cell is either activated or not. The dynamic interaction between activation and inhibition, an essential factor determining the viability of the population, is captured through a system of differential equations. For simplicity, we use terms that are not technical so that the model can be understood by researchers in different disciplines. We introduce the variables involved in our model:

$L$ - total number of free (not docked) activating molecules.

$X$ - total number of free (not docked) molecules of the inhibiting substance.

$R$ - total number of unoccupied 'docking' places on the sensors where $X$ or $L$ can attach

$P$ - total number of docking places on the sensors occupied by activating molecules $L$.

$Q$ - number of docking places on the sensors occupied by the inhibiting substance molecules $X$.

All these quantities are dynamic in the sense that they vary with time. A summary of how these quantities interact is shown in Fig. 2.

The activation and blocking of the sensors can be described by equations similar to that used in chemical reactions:

$$R + L \underset{k_{-1}}{\overset{k_1}{\rightleftharpoons}} P \tag{1}$$

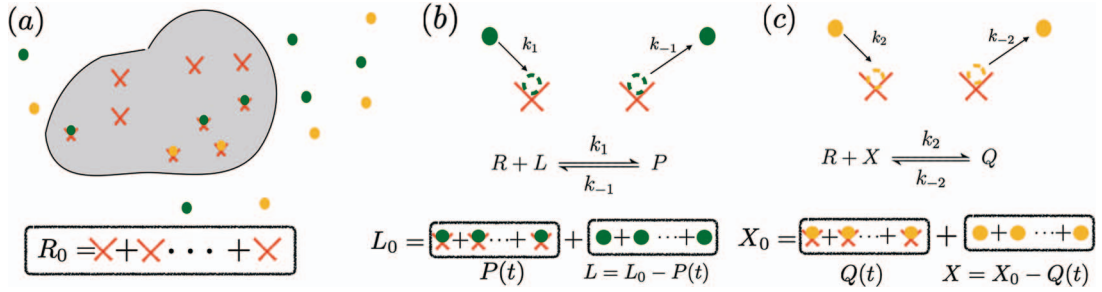$$R + X \underset{k_{-2}}{\overset{k_2}{\rightleftharpoons}} Q \tag{2}$$

FIG. 2. Kinetics: docking places (red), activating molecules (green) and inhibiting molecules (yellow) (a). Sensors (docking places) on a cancer cell. (b) and (c) Chemical reactions along with the relationship between dynamic and static quantities.

The constants $k_1$ and $k_{-1}$ are specific for the activator, namely the considered here CXCL12 molecule, while $k_2$ and $k_{-2}$ are specific for the inhibiting agent. These reactions can be represented by the following differential equations using the principle of mass action reaction kinetics:

$$\frac{dP}{dt} = k_1 RL - k_{-1} P \tag{3}$$

$$\frac{dQ}{dt} = k_2 RX - k_{-2} Q, \tag{4}$$

$$\frac{dL}{dt} = -k_1 RL + k_{-1} P, \tag{5}$$

$$\frac{dX}{dt} = -k_2 RX + k_{-2} Q, \tag{6}$$

$$\frac{dR}{dt} = -k_1 RL - k_2 RL + k_{-1} P + k_{-2} Q. \tag{7}$$

By adding the appropriate equations we obtain

$$\frac{d(P+L)}{dt} = \frac{d(Q+X)}{dt} = \frac{d(P+Q+R)}{dt} = 0. \tag{8}$$

Hence, the quantities $P+L$, $Q+X$, $R+P+Q$ remain constant during the reactions (1)–(2). This should not be surprising since these reactions do not consider any growth or decay in the total number of molecules of the activating agent, the inhibiting substance and docking places on the sensors. We have

$L_0 := P + L =$ total number of activating molecules, docked or free;

$X_0 := Q + X =$ total number of molecules of the inhibiting substance, docked or free;

$R_0 := P + Q + R =$ total number of docking places on the sensors occupied by

activating molecules, occupied by the inhibiting substance or free.

It is possible to consider the processes of generation and destruction of the activating molecules as well as destruction and re-supply of the inhibiting substance. However, considering these quantities as constants may be sufficient as a first step as well as relevant to the conducted experiments due to their limited time span.

Substituting $L = L_0 - P$, $X = X_0 - Q$ and $R = R_0 - P - Q$ into equations (3)–(4), we obtain system of two equations only:

$$\frac{dP}{dt} = k_1(R_0 - P - Q)(L_0 - P) - k_{-1}P, \tag{9}$$

$$\frac{dQ}{dt} = k_2(R_0 - P - Q)(X_0 - Q) - k_{-2}Q. \tag{10}$$

## 2.2 Equilibrium of the inhibition dynamics

We describe the qualitative dynamics of the system of differential equations (9)–(10). The only set of initial conditions that are physically plausible is the set

$$\Omega := \{(P, Q) : 0 \le P \le L_0,\ 0 \le Q \le X_0, P + Q \le R_0\}. \tag{11}$$

The following theorem shows that for all solutions of (9)–(10) initiated in $\Omega$, the activation level, as given by the value of $P$ and the inhibition level, as given by the value of $Q$, approach an equilibrium as time increases. The practical message is that if the assumed conditions remain prevalent in the long term, the inhibition level approaches a constant.

THEOREM 1. Consider the dynamical system (9)–(10) with all parameters being positive as well as the set $\Omega$ as defined in (11). Then the following results hold:

  (i) There is a unique equilibrium point $(P^*, Q^*)$ in the interior of $\Omega$.

 (ii) The equilibrium $(P^*, Q^*)$ is a stable proper node and hence locally asymptotically stable.

(iii) The set $\Omega$ is positively invariant, that is for any initial condition $(P(0), Q(0)) \in \Omega$ the solution $(P(t), Q(t))$ of the system (9)–(10) is defined for all $t > 0$ and $(P(t), Q(t)) \in \Omega, t > 0$.

(iv) The set $\Omega$ is contained in the basin of attraction of $(P^*, Q^*)$.

Note that the statement (iv) in Theorem 1 is stronger than saying $\Omega$ is positively invariant, while statement (ii) or (iii) does not specify the basin of attraction of $(P^*, Q^*)$. The proof of Theorem 1 is presented in the Appendix.

The phase diagram on Fig. 3 shows how the trajectories of the solutions of the system (9)–(10) approach the equilibrium $(P^*, Q^*)$, as stated in Theorem 1. One can further observe that all trajectories initiated at the boundary of $\Omega$ excluding the origin are tangential to the line

$$P + Q = P^* + Q^* \tag{12}$$

at the equilibrium. More precisely, the trajectories first approach the mentioned line (12) and then continue towards the equilibrium while getting closer to the line and becoming visually indistinguishable from it. This type of dynamics occurs when the Jacobian of the vector field at the equilibrium has two
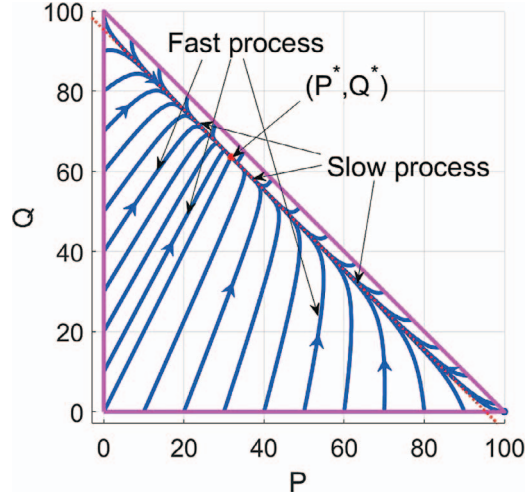
FIG. 3. Phase diagram of the models (9)–(10) of activation ($P$) and inhibition ($Q$) with parameter values $(R_0, L_0, X_0, k_1, k_2, k_{-1}, k_{-2}) = (100, 100, 200, 10, 10, 1, 1)$. The domain $\Omega$ is the set with the purple boundary. The shape of the trajectories is determined by the interaction of the fast and slow processes: except for the fast manifold, all other trajectories first approach the slow manifold and than converges to the equilibrium $(P^*, Q^*)$ tangentially to the slow manifold. The parameters satisfy the condition (16). Hence, the fast and the slow manifold are straight lines given by (20) and (21), respectively.

distinct negative eigenvalues as captured in the concept *stable proper node* (Tabor, 1988, Section 1.4). The next subsection discusses the physiological and the mathematical aspects of such dynamics.

### 2.3 *Fast and slow manifolds*

We can rewrite the systems (9)–(10) in the form

$$\frac{dP}{dt} = k_1 R_0 \frac{R_0 - P - Q}{R_0}(L_0 - P) - k_{-1}, P \tag{13}$$

$$\frac{dQ}{dt} = k_2 R_0 \frac{R_0 - P - Q}{R_0}(X_0 - Q) - k_{-2}Q. \tag{14}$$

We next set $\tilde{k}_i = k_i R_0$, with $i = 1$ or $i = 2$ and along with $k_{-1}, k_{-2}$ these quantities are all rates where the measuring unit is 'per unit time'. Specifically, $\tilde{k}_1$ is the rate of attachment of the activating agent and $\tilde{k}_2$ is the rate of attachment of the inhibiting agent when all docking places are free ($P = Q = 0$). Typically in the described type of physiological processes and as it is the case with activation (by CXCL12) or blocking (by an inhibiting agent, e.g. L-kynurenine) of the receptor CXCR4, we have

$$\tilde{k}_1 \gg k_{-1}, \quad \tilde{k}_2 \gg k_{-2}. \tag{15}$$

The attachment rate is reduced by the fraction of available docking places, that is $\frac{R_0 - P - Q}{R_0}$ (dimensionless). When many docking spaces are available, that is $P + Q$ is small compared to $R_0$, we have a fast process of attachment (growth of both $P$ and $Q$) driven by $\tilde{k}_{1,2}$. When the docking places are near full,

the rates of change in $P$ and $Q$ depend on the rate new docking spaces become available, that is by $k_{-1}$ and $k_{-2}$. Considering (15), this is relatively much slower process.

The fast and the slow processes are represented mathematically by the invariant manifolds associated with the eigenvalues of the Jacobian of the right-hand side of the system (9)–(10). As shown in the proof of Theorem 1 (see Appendix), the Jacobian has two distinct negative eigenvalues. Let us denote them by $-\lambda$ and $-\mu$, where $\mu > \lambda > 0$. It follows easily from the invariant manifold theory, e.g. (Wiggins, 2003, Theorem 3.2.1), that there exists locally a one-dimensional invariant manifold corresponding to each eigenvalue. More specifically, each invariant manifold is a smooth curve passing through the equilibrium and tangent to the eigenvector of the respective eigenvalue. The invariantness further implies that each of these curves is a trajectory of a solution. Any non-equilibrium solution as time decreases can be extended to intersect the boundary of $\Omega$ in view of Theorem 1. The manifold (curve) corresponding to the eigenvalue $-\lambda$ represents the slow process, while the manifold (curve) corresponding to the eigenvalue $-\mu$ represents the fast process. Hence, we refer to them as the slow manifold and the fast manifold, respectively. Any solution that is not initiated on any of the two manifolds displays features of both, with the dynamics on the slow manifold eventually dominating.

The separation of the fast and the slow dynamics is a powerful tool in the analysis of complex models in many fields, including chemical kinetics (Bykov & Goldshtein, 2013). The underlying mathematics is the singular perturbation theory (Verhulst, 2010, Section 8.2), further generalized to arbitrary vector fields in Bykov *et al.* (2006). This theory demonstrates that the slow processes are (mostly) responsible for the long-term or limiting dynamics. Hence, the analysis can be reduced (with some approximation error) to the analysis of the system on the slow manifold (Bykov & Goldshtein, 2013).

In the special case when

$$k_1 = k_2, \quad k_{-1} = k_{-2} \tag{16}$$

and using the results in the Appendix, one can derive the values of $\lambda$ and $\mu$ in the following explicit form

$$\lambda = k_1(R_0 - P^* - Q^*), \quad \mu = \lambda + k_1(L_0 + X_0 - P^* - Q^*). \tag{17}$$

Clearly, $\lambda < \mu$. Further, it is easy to show that

$$\lambda < k_{-1}\left(1 + \frac{R_0}{L_0 + X_0 - R_0}\right), \tag{18}$$

$$\mu > \lambda + \tilde{k}_1 \frac{L_0 + X_0 - R_0}{R_0}. \tag{19}$$

The upper bound of $\lambda$ in (18) is directly proportional to $k_{-1}$ indicating that $\lambda$ is small when $k_{-1}$ is small. Similarly, the lower bound of $\mu$ in (19) indicates that $\mu$ is significantly larger than $\lambda$ when $\tilde{k}_1$ is large. One should note that increasing $X_0$ does not change the situation. In fact, the upper bound of $\lambda$ decreases with respect to $X_0$, while the lower bound of $\mu$ increases, making the difference between the fast and the slow processes even more pronounced.
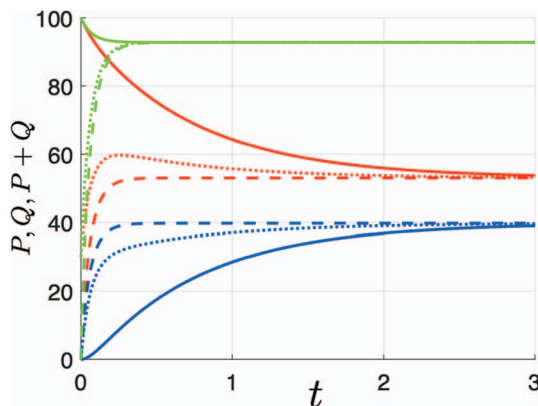
FIG. 4. Graphs of the solutions $P$ (red)and $Q$ (blue) of the models (9)–(10) as well as $P + Q$ (green) as functions of time ($t$). The values of the parameters are as for Fig. 3, namely $(R_0, L_0, X_0, k_1, k_2, k_{-1}, k_{-2}) = (100, 100, 200, 10, 10, 1, 1)$, for varied set of initial conditions. The graph of $P + Q$ approaches the equilibrium considerably more quickly than either $P$ or $Q$, i.e. it is forming a boundary layer as in singular perturbation theory (Verhulst, 2010), and motivates reducing the analysis of model to its slow manifold.

In this specific case, both the slow manifold (associated with $\lambda$) and the fast manifold (associated with $\mu$) are straight lines with respective equations

$$P + Q = P^* + Q^*, \tag{20}$$

$$Q^*P - P^*Q = 0. \tag{21}$$

These straight lines are visible on Fig. 3, where the parameters are such that (16) holds. The temporal dynamics are illustrated on Fig. 4. Compared to the graphs of $P(t)$ and $Q(t)$, the graph of $P(t) + Q(t)$ converges to its equilibrium much faster. Considering (20), this indicates the convergence of the solutions $P(t), Q(t)$ to the slow manifold that is much faster than the convergence to their equilibrium values. This is a different way of representing the property that

*all solutions, excluding the one initiated at the origin, eventually approach the*

*equilibrium of the system on a trajectory indistinguishable from the slow manifold.* (22)

The special case when (16) holds was considered in some detail to illustrate the ideas that extend to the general case, i.e. when (16) is not true. The behavior of the solution in the general case is determined (as stated in (22)) by a fast and slow manifolds associated with the equilibrium as long as (15) holds. Figure 5 represents a phase diagram for different values of the rate constants where (16) does not hold. The fast manifold, the slow manifold and the property (22) can be observed in the figure.

## 3. Experimental data

The inhibitor compound used in this study is L-Kynurenine (L-Kyn). L-Kyn, a downstream metabolite of the amino acid tryptophan, has been shown to inhibit proliferation and induce cell death of melanoma
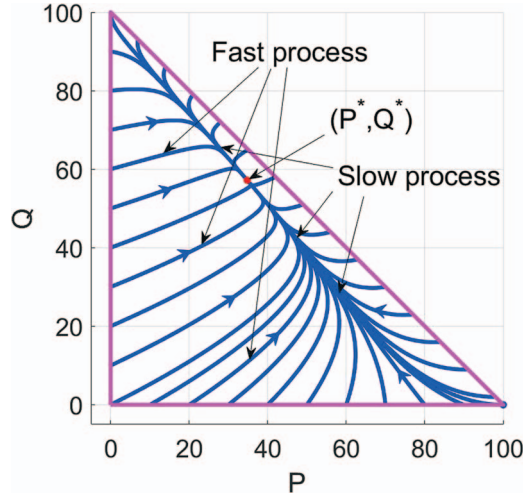
FIG. 5. Phase diagram of the models (9)–(10) of activation ($P$) and inhibition ($Q$) with parameter values $(R_0, L_0, X_0, k_1, k_2, k_{-1}, k_{-2}) = (100, 100, 200, 20, 5, 3, 1)$. The domain $\Omega$ is the set with the purple boundary. The parameters do not satisfy the condition (16). Hence, the fast and the slow manifold do not have simple equations as in (20) and (21). Nevertheless, the shape of the trajectories is determined by the interaction of the fast and slow processes: except for the fast manifold, all other trajectories first approach the slow manifold and then converge to the equilibrium ($P^*, Q^*$) tangentially to the slow manifold.

cell-lines via *in vitro* studies (Walczak *et al.*, 2020). In addition to being an endogenous derivative, L-Kyn is thereby a biologically suitable compound to be tested via melanoma-related *in vitro* assays and to demonstrate a reduction in cell viability at increasing concentrations while still being tolerated by non-cancerous cells (Marszalek-Grabska *et al.*, 2021).

Melanoma cells were exposed to L-Kyn at 1-4 milli molars (mM) for 24, 48 and 72 hours. The cells were then tested for cell viability using the crystal violet assay. The goal is to measure the effect of the inhibitory agent on cell viability. Theoretically, the cell viability of a treated population is a function of time. At any given time, it is defined as the ratio of the treated population size over the size of this population if untreated. Following the crystal violet assay (Feoktistova *et al.*, 2016), the cell viability is measured as follows. A set of wells is prepared with 5000 cells each in growth cell culture medium and incubated at physiological conditions. The initial size of the population is verified via manual counting. After one day all cells are attached to the wells. The wells are divided into groups: control (no inhibition), positive control (a known inhibitor added—nocodazole (NOC)) and the other groups treated with varied concentrations of the inhibiting agent (L-Kyn). At least 9 wells from each group are analysed in 24 hours, 48 hours and 72 hours. The cells are fixed in their state, treated with crystal violet dye (absorbed only by the DNA of living cells), and the wells are washed so that only the attached cells remain. Then the absorbance of the dye is measured. The cell viability is calculated as the ratio of the absorbance of the treated population over the absorbance the control population.

As expected due to the reasons given in the introduction, variations of the measurements are observed in each analysed set of treated populations as well as in the populations in the negative control group, i.e. the untreated. The calculated cell viability versus concentration of L-Kyn is given in Fig. 6(a)–(c) for the specified measurement times. Every point is calculated using the average of three wells. The percentage is taken with respect to the control populations so that the control population is always 100%. At least three experiments were conducted. The graphs on Fig. 6(a)–(c) demonstrate significant variability of the results
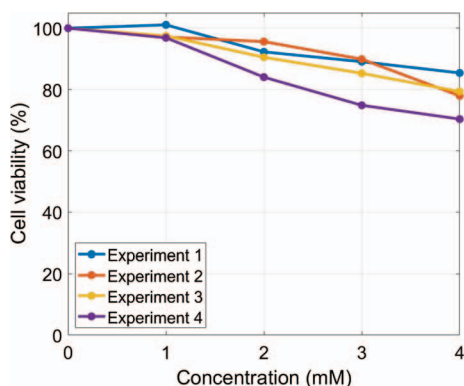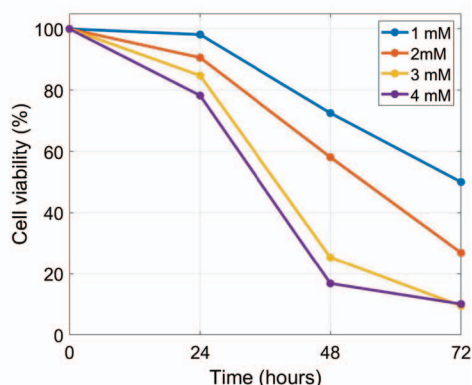
(a) Cell viability at 24 hours.
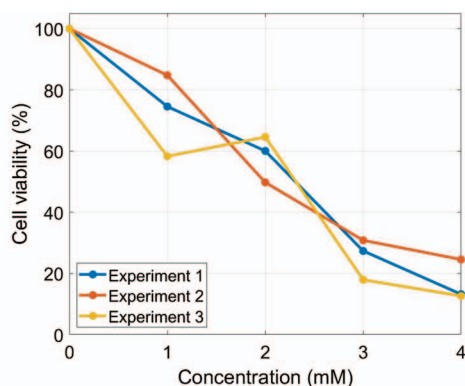
(b) Cell viability at 48 hours.
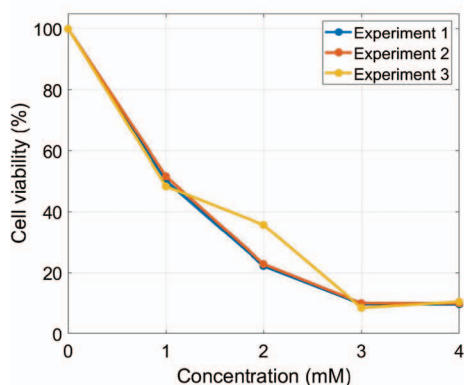
(c) Cell viability at 72 hours.

(d) Average cell viabilities over time for the different concentrations of L-Kyn.

Fig. 6. Graphs showing experimental data for concentrations of the inhibitor (L-Kyn) at 1 mM, 2 mM, 3 mM and 4 mM at the time points of 24 hours, 48 hours and 72 hours that were obtained using the crystal violet assay. For each time point, at least three experiments are carried out. Variability across experiments can be observed on (a), (b) and (c), where segments of the same color connect data collected in the same experiment. Trends of how the cell viability depends on time and concentration emerge clearer on the time diagram (d) of the averaged data.

from one experimental series to the next. The main reason for this variability is that no two measurements can be taken from the same population. However, trends can be extracted when considering large number of experiments. The simplest way to integrate data at the same time under the same treatment is by using the mean. Figure 6(d) represented the average cell viability versus time for the three concentrations in the experiments. One can observe that there are general trends of decreasing of cell viability with respect to time and with respect to concentration. Quantifying these general trends only from the data, particularly considering the mentioned variability and some apparent exceptions from these trends, is not likely to be very reliable. In the sequel, we suggest a method of integrating the data over time using the models (9)–(10). In this way, the data is considered in its entirety over time and not only at individual time instances.

## 4. Expanding the model: theoretical derivation of the cell viability

We associate the data discussed in Section 3 with the models (9)–(10) in the following way. In this section, we construct mathematically the concept of cell viability as a function of time using the theoretical definition discussed already. In the sections that follow, we consider the assay data as approximate measurements of the value of this function at given times, so that reliable and accurate approximation of this function is derived.

Let $M(t)$ denote the size of a natural population of cells. Suppose that sufficient resources and optimal environment (as in the assay) are provided. Under such condition, one may assume a constant growth rate model for the population, that is $M(t)$ is a solution of the differential equation

$$\frac{dM}{dt} = rM, \tag{23}$$

where $r > 0$ is the constant (relative) growth rate. Then we have

$$M(t) = M(0)e^{rt}.$$

Let $\widehat{M}(t)$ denote the size of an identical at $t = 0$ population of cells, which is subjected to some treatment. In the setting of the models (9)–(10), the treatment is inhibition through the blocking of the CXCR4 sensor. Then the cell viability is the function

$$\frac{\widehat{M}(t)}{M(t)}, \tag{24}$$

where the fraction is expressed as a percentage. For every concentration, the data in Section 3 can be considered as a set of measurements of this function at times $t = 0$, $t = 24$, $t = 48$, $t = 72$ hours. We can interpret the error of the measurements in different ways. In whichever way we consider the measurements and the error associated with them, the goal is to derive an approximation to the function (24), which agrees best with the data. For that goal, first we derive from the models (9)–(10) a suitable representation of (24).

The impact of the inhibition can be modelled either as a function of $Q$ or as a function of $P$. We chose here $Q$. The inhibition $Q$ is expected to reduce the growth rate. Thus, we have

$$\frac{d\widehat{M}}{dt} = (r - \alpha Q(t))M, \tag{25}$$

where $\alpha$ is a positive constant. If the function $Q$ is known, equation (25) can be solved explicitly and we have

$$\frac{\widehat{M}(t)}{M(t)} = \frac{M_0 e^{rt - \alpha \int_0^t Q(\theta)\, d\theta}}{M_0 e^{rt}} = e^{-\alpha \int_0^t Q(\theta)\, d\theta}. \tag{26}$$

Interestingly, the cell viability function does not depend on the constant $r$, while it depends through $Q$ on the values of $k_1, k_{-1}, k_2, k_{-2}, L_0, R_0, X_0, P(0), Q(0)$ in (9)–(10) of which only $X_0$, the concentration of the inhibiting substance, is under the gambit of the experimenter.

In the setting of the experiments, we have $Q(0) = 0$. However, as discussed earlier, driven by the fast process, the solution is very quickly close to the slow manifold. This motivates the validity of approximating such a solution with a solution on the slow manifold, essentially reducing the dimensionality of the system to one, namely a differential equation about $Q$. As an illustration, let us use again the case when (16) holds. Then the slow manifold is the straight-line (20) and $Q$ satisfies on this manifold the differential equation

$$\frac{dQ}{dt} = k_1(R_0 - P^* - Q^*)(X_0 - Q) - k_{-1}Q$$

with the solution given by

$$Q(t) = Q^* - (Q^* - Q(0))e^{-\lambda t},$$

where $\lambda = k_1(R_0 - P^* - Q^*) + k_{-1}$. Hence, the $Q$-coordinate of a solution of the system (9)–(10) can be approximated by

$$Q(t) \approx Q^* - (Q^* - \bar{Q})e^{-\lambda t}, \tag{27}$$

where $(\bar{P}, \bar{Q})$ is appropriate point on the slow manifold.

This approximation is illustrated in Fig. 7(a) for a sample of solutions. One can observe that the graph of the approximation becomes indistinguishable from the $Q(t)$ at about the same time when the graph of $P + Q$ is indistinguishable from its equilibrium, that is the solution is practically on the slow manifold. This happens in a relatively small period of time compared to the time it takes for $Q(t)$ to reach its equilibrium $Q^*$ (the red dashed line). The validity of the approximation of the form (27) can be graphically tested by plotting $\ln(Q^* - Q(t))$. If (27) is valid, then graph of

$$\ln(Q^* - Q(t)) \approx \ln(Q^* - \bar{Q}) - \lambda t,$$

is approximately a straight line. The inverse is also true. If the graph of $\ln(Q^* - Q(t))$ is approximately a straight line, then $Q$ can be approximated as in (27).

In a general model, where (16) does not necessarily hold, approximation of the form (27) in a sufficiently small neighborhood of the equilibrium follows from the Hartman–Grobman Theorem. However, the validity over the whole slow manifold can be tested by plotting the graph of $\ln(Q^* - Q(t))$. Figure 8(a) represents the graphs of $Q$ for a set of solutions of the models (9)–(10) with parameter values as for Fig. 5. On Fig. 8(b), the graphs of $\ln(Q^* - Q(t))$ for the same solutions are given. Similar to Fig. 7(b), these are straight lines except for a small time interval in the beginning. In all our numerical experiments, we found this to be true as long as (15) holds. Hence, we use the approximation (27) with $\bar{Q}$ and $\lambda$ yet unknown.

Then, from (26), we obtain

$$\frac{\widehat{M}(t)}{M(t)} \approx e^{-\alpha Q^* \frac{e^{-\lambda t} - 1 + \lambda t}{\lambda} - \alpha \bar{Q} \frac{1 - e^{-\lambda t}}{\lambda}}. \tag{28}$$

The function in (28) depends on many unknown parameters. These include $\alpha$ and through $Q^*$ and $\bar{Q}$, all parameters of (9)–(10) as well as $P(0)$. Hence, this function is not intended to be derived from the model,
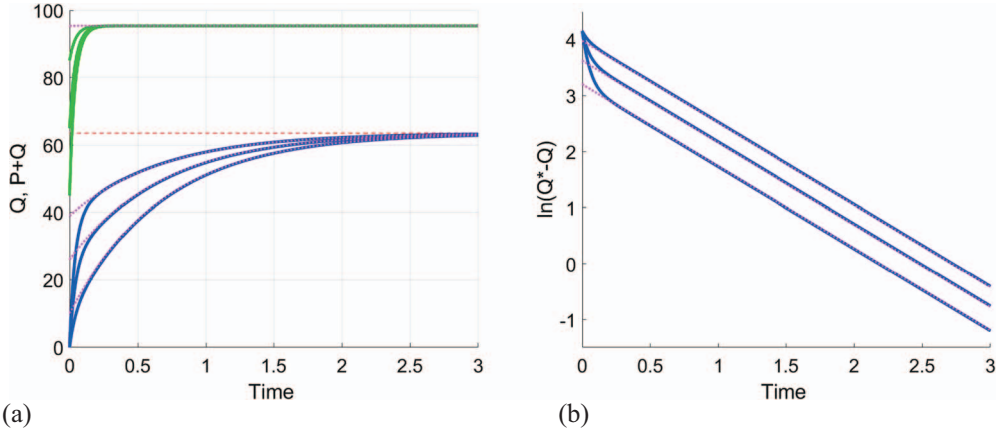
FIG. 7. Solutions of models (9)–(10) with parameters $(R_0, L_0, X_0, k_1, k_2, k_{-1}, k_{-2}) = (100, 100, 200, 10, 10, 1, 1)$ (as in Fig. 3) and initial conditions $Q(0) = 0$, $P(0) \in \{45, 65, 85\}$ (a) Graphs of the $Q$-coordinate (solid blue) of solutions and their approximations on the slow manifold (dotted magenta). Graphs of $P + Q$ (solid green) for the same solutions. The graphs of $P + Q$ reach equilibrium relatively fast, thus indicating a boundary layer as in Fig. 3. Except for a short initial time period, the graph of $Q$ overlaps with its approximation on the slow manifold. (b) Graphs of $\ln(Q^* - Q)$ for the functions $Q$ (solid blue) and their approximations (dotted magenta) plotted in (a). Except for a short initial time period the graph of $\ln(Q^* - Q)$ is a straight line, thus indicating exponential decay.
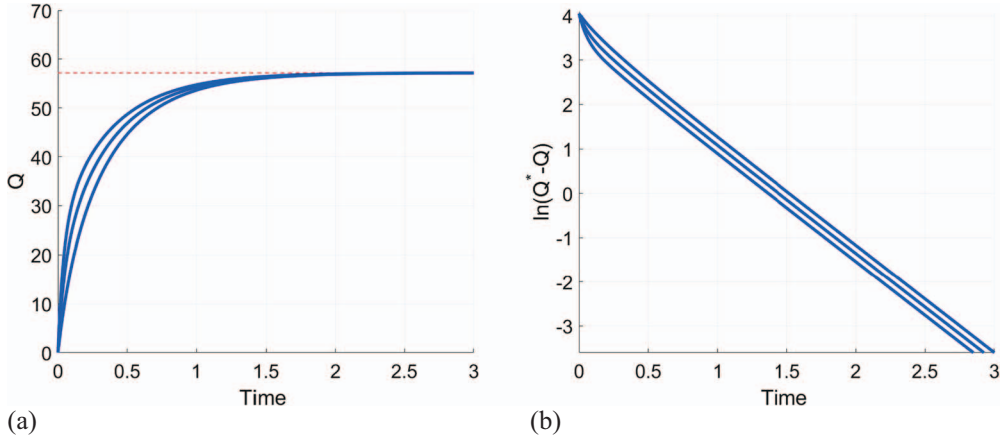


FIG. 8. Solutions of models (9)–(10) with parameters $(R_0, L_0, X_0, k_1, k_2, k_{-1}, k_{-2}) = (100, 100, 200, 20, 5, 3, 1)$ (as in Fig. 5) and initial conditions $Q(0) = 0$, $P(0) \in \{25, 50, 75\}$. (a) Graphs of the $Q$-coordinate (solid blue) of solutions. (b) Graphs of $\ln(Q^* - Q)$ for the functions $Q$ (solid blue) and their approximations (dotted magenta) plotted in (a). Since (8) is violated, we do not have the approximation on the slow manifold in an explicit form. Nevertheless, except for a short initial time period, the graph of $\ln(Q^* - Q)$ is a straight line, thus indicating exponential decay and motivating approximation by (27).

but rather it provides means of assimilating the data as approximate observations of a function of specific form. Taking into account that, as discussed in Section 3, some error is involved in the measurements, we may consider that measurements of $\frac{\hat{M}(0)}{M(0)}$, while close to 1 are not necessarily 1. Then we have for

the cell viability an approximation by a function of the form

$$\frac{\widehat{M}(t)}{M(t)} \approx \phi(t) = Ae^{-B\frac{e^{-\lambda t}-1+\lambda t}{\lambda}-C\frac{1-e^{-\lambda t}}{\lambda}}, \tag{29}$$

where $A \approx \frac{\widehat{M}(0)}{M(0)} = 1$, $B = \alpha Q^*$, $C = \alpha \bar{Q}$. The values of $A$, $B$, $C$ and $\lambda$ for each concentration of the inhibiting agent can be estimated by fitting the curve $\phi$ to the experimental data.

**Remark.** The time scale on Figs 4, 7 and 8 is not specified. These figures represent qualitatively the behavior of the depicted functions over time. Note that the conclusions derived from these figures are of such nature that they are independent of the time scale. The time axis on Figs 4, 7 and 8 should not be confused with the time axis on Fig. 6(d) as well as figures in the next sections, where the time is in hours and the range is determined by the measurement times in the experiments.

## 5. Identifying the parameters of the cell viability function from the experimental data

### 5.1 *Fitting curves of the form (28) to the experimental data*

We consider the data discussed in Section 2, which was obtained via the crystal violet assay protocol using L-Kyn as an inhibiting agent. For any fixed concentration, we use the least squares method to derive the best fitting curve of the form (29), where at $t = 0$ we consider the square of $\phi(0) - 1 = A - 1$. The optimization was performed using the Matlab function `fminsearch` (MATLAB, 2010), with starting points from a dense mesh covering the feasible domain of the parameter vector $(A, B, C, \lambda)$. The numerical procedure discovered multiple local equilibria with very similar values of the objective function, but very different values of the parameters. Further, all runs returned small values of $\lambda$ (not exceeding $10^{-3}$), which explains the ill-conditioning of the optimization problem. For small $\lambda t$, the first fraction in the exponent in (29) is approximately equal to $\frac{1}{2}\lambda t^2$. Hence, $B$ and $\lambda$ cannot be reliably estimated, e.g. increase in $B$ can be compensated by a decrease of $\lambda$, returning the same or very similar value of the objective function. This is resolved by rewriting the function $\phi$ in the form

$$\phi(t) = Ae^{-D\frac{e^{-\lambda t}-1+\lambda t}{\lambda^2}-C\frac{1-e^{-\lambda t}}{\lambda}}, \tag{30}$$

where $D = \lambda B$. This stabilizes the optimization problem and we obtain a unique equilibrium for every concentration. The values of $A$, $D$ and $\lambda$ are given in Table 1, while the graphs of $\phi$ are presented in Fig. 9. Let us recall that the statistic $R^2$ measures the goodness of fit of a model. It represents the fraction of variation explained by the model. Therefore, it varies between 0 and 1. Values over 0.95, as the values obtained in Table 1, are considered to indicate a very good fit of the model to the data.

### 5.2 *Analysis and interpretation*

The main driver of the dynamics of the curves in Fig. 9 is the term the parameter $D = \alpha\lambda Q^*$. Considering the mathematical definition and the biological meaning of $Q^*$ and $\lambda$, they should both increase with any increase of the concentration of the inhibiting agent. Hence, one expects that $D$ to increase too. Indeed, such increase of $D$ can be observed clearly in Table 1.

The parameter $C = \alpha\bar{Q}$ is expected to have similar values for all experiments since the initial states are similar. The obtained values of $C$ are in a short-range near zero, from $10^{-14}$ to $10^{-16}$. These small values of $C$ imply that the initial states of the system are very close to the endpoint at $Q = 0$ of the
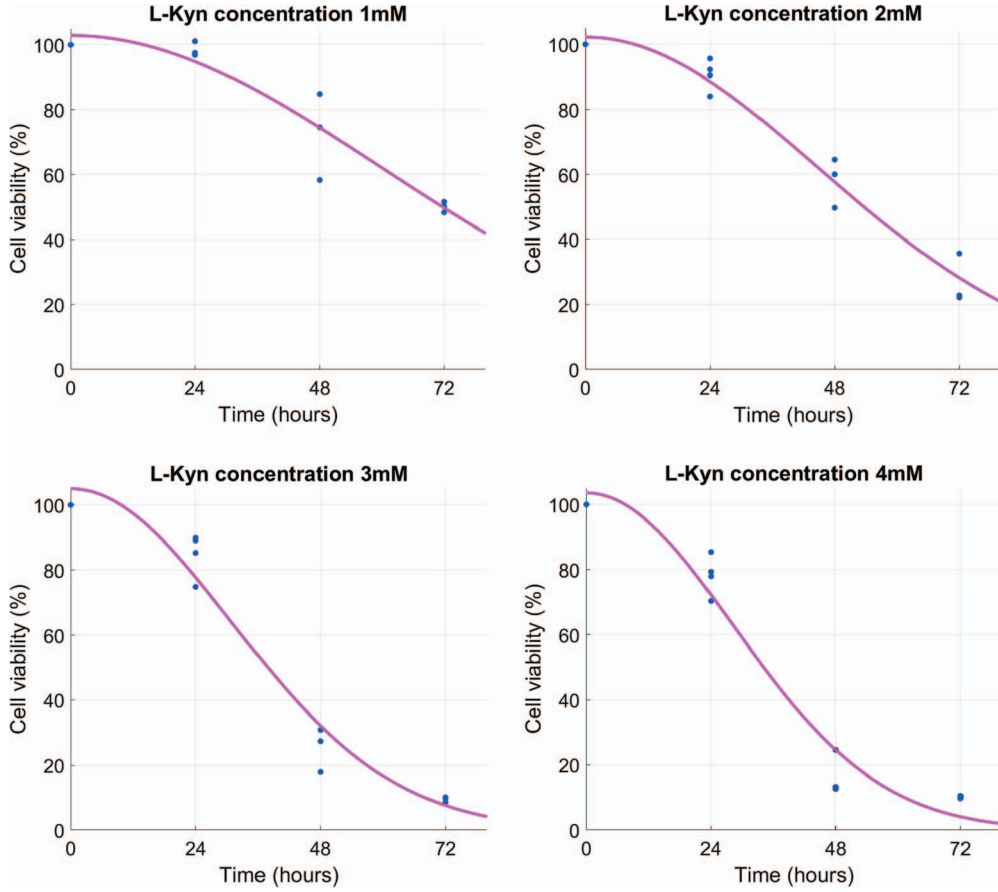
FIG. 9. Graphs (solid magenta) of the functions of the form (30) fitted to the data of cell viability with concentration of the inhibitor (L-Kyn) at 1 mM, 2 mM, 3 mM and 4 mM at the time points of 24 hours, 48 hours and 72 hours (see Fig. 6). The blue dots represent the data points.

TABLE 1    *Estimated values of the parameters A, D, C and λ in (30)*

| Concentration | $A$ | $D$ | $C$ | $\lambda$ | $R^2$ |
|---|---|---|---|---|---|
| 1mM | 1.02866 | $2.82646 \times 10^{-4}$ | $1.47370 \times 10^{-14}$ | $3.19765 \times 10^{-4}$ | 0.9665 |
| 2mM | 1.02222 | $4.97166 \times 10^{-4}$ | $3.22590 \times 10^{-14}$ | $8.55739 \times 10^{-5}$ | 0.9794 |
| 3mM | 1.04992 | $1.05762 \times 10^{-3}$ | $1.40822 \times 10^{-15}$ | $1.75403 \times 10^{-3}$ | 0.9710 |
| 4mM | 1.03818 | $1.27147 \times 10^{-3}$ | $5.91781 \times 10^{-16}$ | $1.55132 \times 10^{-3}$ | 0.9691 |

slow manifold. We recall that in the implemented experiments, the cells were allowed to settle under optimal conditions for 24 hours. One may expect that during this period large fraction of the receptors CXCR4 were occupied by the CXCL12 molecules. A small value of $C$, and respectively of $\bar{Q}$, support this hypothesis.
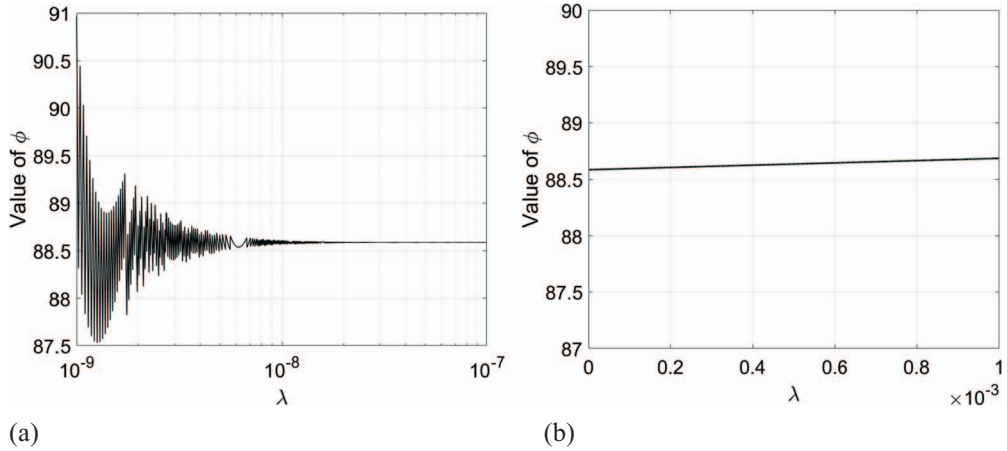
FIG. 10. Graphs of $\phi$ as the function of $\lambda$ with the other parameters as for concentration 2mM in Table 1 and $t = 24$: (a) The value of the function $\phi$ cannot be computed accurately for $\lambda < 10^{-7}$ (log scale for $\lambda$) using the formula (30) on a digital computer with double precision. As $\lambda \to 0$, the value of $\phi$ monotonically decreases to 88.585...%. The graph shows oscillations and lack of convergence, thus illustrating the loss of accuracy. (b) The graph exhibits a very small gradient for $\lambda \in [10^{-7}, 10^{-3}]$, i.e. $\phi$ is nearly constant with respect to $\lambda$. The graphs in (a) and (b) motivate the using the approximation (31).

Regarding the estimated values of $\lambda$, firstly let us note that they are small. Using $\bar{Q} \approx 0$, we have

$$Q(t) \approx (1 - e^{-\lambda t})Q^*.$$

The small values of $\lambda$ indicate that the observed impact on cell viability occurs while $Q(t)$ is still relatively far from its equilibrium. As an example, for the concentration of 3mM, $Q(72) \approx 0.118Q^*$, that is the level of inhibition is about 12% of its maximum for the given concentration.

Secondly, we can observe that in this range of $\lambda$ of about $10^{-3}$ and less, the function $\phi$ depends little on $\lambda$. As an example, we have on Fig. 10(b) the graph of $\phi$ as a function of $\lambda$ with the rest of the parameters being for the concentration 2mM and $t = 24$. There is indeed a very small gradient, which implies that the estimates of $\lambda$ are sensitive to small variations of the data. A general decreasing trend in the values of $\lambda$ can be noticed in Table 1, but it is not as clear and well pronounced as in the case of $D$. The mentioned sensitivity is a possible reason. From Fig. 10(a), we observe that for even smaller values of $\lambda$ ($\lambda < 10^{-7}$) the accuracy of the computation of $\phi$ is completely lost due to roundoff errors.

### 5.3  *Reducing the number of parameters*

Theoretically, function $\phi$ depends on four parameters. However, we established little dependence on $\lambda$. More precise computations show that, we have

$$\frac{e^{-\lambda t} - 1 + \lambda t}{\lambda^2} \approx \frac{1}{2}t^2, \tag{31}$$

where for $\lambda < 0.002$ and $t \leq 72$, the relative error of approximation is bounded above by

$$\frac{1}{3}\lambda t < 4.8\%. \tag{32}$$

TABLE 2    *Estimated values of the parameters A and D in (33)*

| Concentration | $A$ | $D$ | $R^2$ |
|---|---|---|---|
| 1mM | 1.02841 | $2.80609 \times 10^{-4}$ | 0.9665 |
| 2mM | 1.02211 | $4.96267 \times 10^{-4}$ | 0.9794 |
| 3mM | 1.04874 | $1.02984 \times 10^{-3}$ | 0.9716 |
| 4mM | 1.03746 | $1.24571 \times 10^{-3}$ | 0.9695 |

Hence, we can apply the approximation formula in (31). Similarly, we have

$$\frac{1 - e^{-\lambda t}}{\lambda} \approx t.$$

However, due to the small value of $C$, the term containing this fraction makes a negligible contribution to the value of $\phi$. Therefore, from a mathematical point of view, the obtained functions $\phi$ can be nearly as well represented through functions from the two-parameter family

$$\psi(t) = Ae^{-\frac{1}{2}Dt^2}. \tag{33}$$

To validate this statement, we repeated the fitting process to the data using the functions $\psi$ as given in (33). The estimated values of $A$ and $D$ are given in Table 2. The values of $D$ are very similar to the values of $D$ in Table 1 with at least the first two significant figures being the same. The values of $A$ are the same correct to four significant figures. The value of $R^2$ has a very small increase affecting the fourth or fifth digit only. The graphs of the functions $\psi$ with parameters from Table 2 are visually indistinguishable from the graphs of the functions $\phi$ on Fig. 9. Hence, these need not be presented.

The form (33) takes into account that the parameters $C$ and $\lambda$ in (30) are confined into a small neighborhood of zero, so that one can get nearly as good approximation using a two parameter family functions as given in (33). The similarity of the approximations by $\phi$ and $\psi$ highlights

- the robustness of the estimation of these two parameters;

- identifying the term $Dt^2$ as a primary driver of the dynamics with respect to time (due to this quadratic term we obtain the distinct sigmoidal shape of the curves in Fig. 9);

- the parameter $D$ captures the response to change of the concentration of the inhibitor.

**Remarks.**

1. The parameter $D = \alpha\lambda Q^*$ is composite and depends on all parameters of the model. While $\lambda$ is removed from $\phi$ as we move from (30) to (33), $\lambda$ is not removed from the cell viability function (28). It is still represented through $D$. Further, the form (33) shows that, while it might be difficult to estimate reliably $Q^*$ and $\lambda$ individually, a reliable estimation of the product comprising $D$ can be computed.

2. The fact that we can reduce the number of parameters of $\phi$ to two by letting $\lambda \to 0$ in the first fraction of the exponent and $C = 0$ is only valid for the considered set of data and it is not a general property of the model. In a different experiment, where a different set of data is obtained, the situation may be different. For example, $\lambda$ is small only relative to the considered time interval
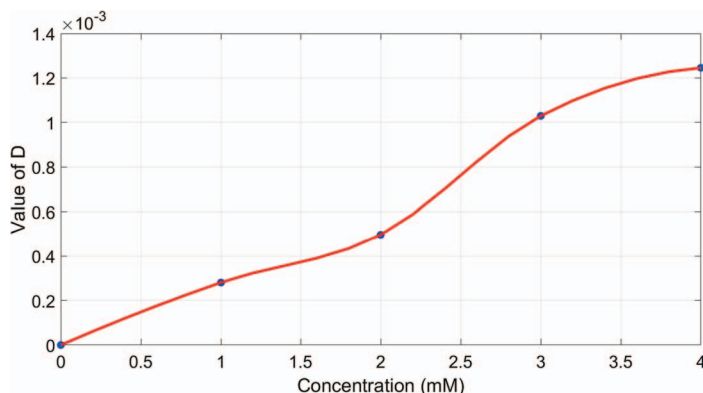
FIG. 11. Graphs of the values of $D$ for $c = 0, 1, 2, 3, 4$ (blue dots) and the interpolating function for $c \in [0, 4]$ (red solid line).

[0, 72] so that (32) holds. If experiments are conducted over a longer period of time, (31) would not be appropriate to use.

3. The parameter $A$ was introduced in (30) to account for possible variation in the initial states of the populations. Indeed, as the cell viability values are calculated based on the controls (cells not exposed to any compound), a variability in the cell viability values are expected even at $t = 0$. The fact that the results in Table 1 and in Table 2 show values of $A$ is persistently larger than 1 by about 3% is a possible indication of a process not yet accounted for in the model. For example, some compounds are known to cause cell growth and not just cell death. An alternative possible cause is a small delay from administering the inhibitor until the processes start progressing exactly as described in the model. The deviation of $A$ from 1 is not sufficiently pronounced to support any of these hypotheses with the available data. Further, the mentioned overestimation of $A$ is rather small to affect the quality of the approximation beyond the initial stages, as the decay due to the exponent in (33) determines the primary dynamics. It is nevertheless an issue that can be investigated in future research theoretically and experimentally.

## 6. Calculating $IC_{50}$

As mentioned, $IC_{50}$ is a commonly used for characterizing the inhibiting properties of an agent and as a benchmark for comparison with other agents. In more detail, given time $t$, $IC_{50}(t)$ is the concentration that reduces the viability of the cells by 50% at time $t$. From the graphs in Fig. 9, given the respective concentration, one can read the time for which this concentration provides a 50% reduction of cell viability. We have $IC_{50}(71.84) = 1$, $IC_{50}(53.69) = 2$, $IC(37.86) = 3$, $IC_{50}(34.20) = 4$. We derive in this section the graph of the $IC_({50})$ as a function of time, so that one read from it the value of $IC_{50}$ for any specific time. For that purpose, we represent the cell viability as a function $\varphi(c, t)$ of concentration $c$ (in mM) of the inhibiting agent and the time $t$ (in hours).

As shown in Section 5, the impact of the concentration of the inhibitor is captured through the change of the parameter $D$ in (33). Let us consider $D$ as a function of $c$, that is $D = D(c)$. The second column of Table 2 gives the values of $D(1)$, $D(2)$, $D(3)$ and $D(4)$. By default, $D(0) = 1$. Since we do not have in any explicit form how $D$ depends on $c$, we would not attempt a curve fitting, but rather use an
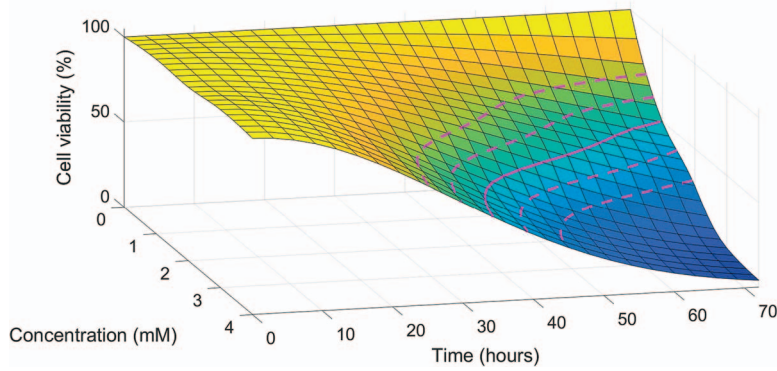
FIG. 12. Surface graph of the cell viability $\varphi$ defined in (34) as a function of two variables—the time and the concentration of the inhibitor. Solid line: level curve at 50%. Dashed lines: level curves at 30%, 40%, 60% and 70%.
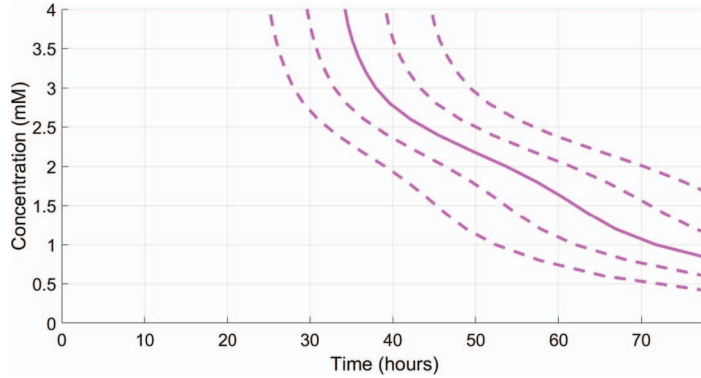


FIG. 13. Solid line: $IC_{50}(t)$ as a function of time. Dashed lines (left to right): $IC_{30}(t)$, $IC_{40}(t)$, $IC_{60}(t)$ and $IC_{70}(t)$ as functions of time.

interpolation of the existing data. One can reasonably expect that the function is $D$ is smooth. Hence, we apply interpolation via cubic convolution—the simplest convolution interpolation, which yields a smooth interpolant (Keys, 1982), and conveniently provided via the Matlab function `interp1` for one dimensional interpolation. The graph of the data points and the interpolating function $D(c)$ for $c \in [0,4]$ is shown in Fig. 11.

In a similar way, we obtain the function $A(c)$ for $c \in [0,4]$. We omit the details since $A$ exhibits little change for different concentrations with respectively little impact on the cell viability.

Thus, we obtain the cell viability function

$$\varphi(c,t) = A(c)e^{-\frac{1}{2}D(c)t^2}, \ c \in [0,4], \ t \in [0,72]. \tag{34}$$

The graph of the viability function $\varphi$ is given on Fig. 12. The magenta solid line on the surface represents the intersection with the horizontal plane where cell viability $= 50\%$. When plotted on concentration vs. time axes, we obtain the graph of the $IC_{50}$ as a function of time, see solid line on

Fig. 13. We can read from the graph $IC_{50}$ for any given time. For example, we have $IC_{50}(48) = 2.2725$, $IC_{50}(60) = 1.638$. Further, since we have the cell viability in the explicit form (34), we can construct a level line at any cell viability level. The dashed lines on Fig. 12 represent level lines for cell viability of 30%, 40%, 60% and 70%. Hence, we can obtain not only the half maximum inhibitory concentration ($IC_{50}$), but also the inhibitory concentration for any required level of cell viability at any specified time. The dashed lines represent the inhibitory concentrations for cell viability of 30%, 40%, 60% and 70% as functions of time.

## 7. Conclusions

The paper represents a study of the inhibition of cancer cell viability via blocking a signalling pathway essential for the adhesion and proliferation of the cells. The method of analysis is based on the derivation of a mathematical model representing the inhibition mechanism and the activation–inhibition dynamics. The experimental results are assimilated and interpreted through the model. Thus, variations in the data that may be obscuring general trends are 'filtered out'. The method is exemplified on blocking the CXCR4/CXCL12 axis in melanoma cells. The experimental data is obtained by using L-Kynurenine as an inhibiting agent. The original contribution of the paper is (a) new model of inhibition of the CXCR12/CXCR4 signalling pathway, comprising a competitive dynamical system; (b) alignment of model and experimental data via theoretical construction of the observable variable, namely the cell viability; (c) quantifying the effect of inhibition in a comprehensive way through the cell viability derived as a function of inhibitor concentration and time. The obtained results enrich the methodology of biological application of mathematical methods and contribute to a better understanding of the inhibition mechanism of signalling pathways. The assessment of the efficiency of the inhibitor is relevant to any further consideration of its feasibility for treatment of melanoma.

Using the same integrative approach of mathematical modelling and experimental work, one can consider other inhibitors. Specifically, this team intends to study the impact of the CTCE-9908 agent as studied by Porvasnik *et al.* (2009) on the cell viability of melanoma cells. However, the method is open to a wider spectrum of applications. Further attention will be given to unveiling any unaccounted yet causal relationships in the model, e.g. the reason for the persistent overestimation of the parameter $A$. Certainly, such work will improve the accuracy of the model and the reliability of the produced results.

## Data availability

All data is graphically represented (i) on Fig. 6(a)–(d) plots of the cell viability vs. inhibitor concentration, and (ii) on Figure Fig. 9(a)–(d) plots of cell-viability vs. time. Numerical values are available from the authors on request.

## References

ALDRIDGE, B. B., BURKE, J. M., LAUFFENBURGER, D. A. & SORGER, P. K. (2006) Physicochemical modelling of cell signalling pathways. *Nat. Cell Biol*, **8**, 1195–1203.

BIASCIA, D., SMORAGIEWICZA, M., CONNELLA, C. M., WANGE, Z., GAOE, Y., THAVENTHIRANA, J. E. D., BASUD, B., LUKASZ MAGIERAA, T., JOHNSONA, I., BAXD, L., GOPINATHANA, A., ISHERWOODA, C., GALLAGHERG, F. A., PAWULAA, M., HUDECOVAA, I., GALEA, D., ROSENFELDA, N., BARMPOUNAKISH, P., POPAI, E. C., BRAISJ, R., GODFREYG, E., MIRK, F., RICHARDSA, F. M., FEARONA, D. T., JANOWITZA, T. & JODRELL, D. I. (2020) Cxcr4 inhibition in human pancreatic and colorectal cancers induces an integrated immune response. *PNAS*, **117**, 28960–28970.

BONILLA, R. V. P., NEKKA, F. & CRAIG, M. (2021) A quantitative systems pharmacology framework for optimal doxorubicin granulocyte colony-stimulating factor regimens in triple-negative breast cancer. *Pharmacology*, **106**, 542–550.

BYKOV, V., GOLDFARB, I. & GOLDSHTEIN, V. (2006) Singularly perturbed vector fields. *J. Phys. Conf. Ser.*, **55**, 28–44.

BYKOV, V. & GOLDSHTEIN, V. (2013) Fast and slow invariant manifolds in chemical kinetics. *Comput. Math. Appl.*, **65**, 1502–1515.

CARDINAL, O., BURLOT, C., YANGXIN, F., CROSLEY, P., HITT, M., CRAIG, M. & JENNER, A. L. (2022) Establishing combination pac-1 and trail regimens for treating ovarian cancer based on patient-specific pharmacokinetic profiles using in silico clinical trials. *Comput. Syst. Oncol.*, **2**, e1035.

CARDONES, A. R., MURAKAMI, T. & HWANG, S. T. (2003) Cxcr4 enhances adhesion of b16 tumor cells to endothelial cells in vitro and in vivo via $\beta 1$ integrin. *Cancer Res.*, **63**, 6751–6757.

CHANG, Y., FUNK, M., ROY, S., STEPHENSON, E., CHOI, S., KOJOUHAROV, H. V., CHEN, B. & PAN, Z. (2022) Developing a mathematical model of intracellular calcium dynamics for evaluating combined anticancer effects of afatinib and rp4010 in esophageal cancer. *Int. J. Mol. Sci.*, **23**, 1763.

CHATTERJEE, S., AZAD, B. B. & NIMMAGADDA, S. (2014) The intricate role of cxcr4 in cancer. *Adv. Cancer Res.*, **124**, 31–82.

DUMORTIER, F., LLIBRE, J. & ARTÉS, J. C. (2006) *Qualitative Theory of Planar Differential Systems*. Springer.

FEOKTISTOVA, M., GESERICK, P. & LEVERKUS, M. (2016) *Crystal Violet Assay for Determining Viability of Cultured Cells*. Cold Spring Harbor Protocols, https://doi.org/10.1101/pdb.prot087379.

HAIBE-KAINS, B., EL-HACHEM, N., BIRKBAK, N. J., JIN, A. C., BECK, A. H., AERTS, H. J. W. L. & QUACKENBUSH, J. (2013) Inconsistency in large pharmacogenomic studies. *Nature*, **504**, 389–393.

HENDRIKS, B. S. (2010) Functional pathway pharmacology: chemical tools, pathway knowledge and mechanistic model-based interpretation of experimental data. *Curr. Opin. Chem. Biol.*, **14**, 489–497.

JENNER, A. L., FRASCOLI, F., YUN, C.-O. & KIM, P. S. (2020) Optimising hydrogel release profiles for viro-immunotherapy using oncolytic adenovirus expressing il-12 and gm-csf with immature dendritic cells. *Appl. Sci.*, **10**, 2872.

KEYS, R. G. (1982) Cubic convolution interpolation for digital image processing. *IEEE Trans. Acoust. Speech Signal Process.*, **29**, 1153 – 1160.

KHINKIS, L. A., LEVASSEUR, L., FAESSEL, H. & GRECO, W. R. (2003) Optimal design for estimating parameters of the 4-parameter hill model. *Nonlin. Biol. Toxicol. Med.*, **1**, 15401420390249925.

LARRAMENDY, M. L. & SOLONESKI, S. (2018) Genotoxicity—a predictable risk to our actual world. *IntechOpen*.

LAYEK, G. C. (2015) *An Introduction to Dynamical Systems and Chaos,* vol. 449. Springer.

LEE, J., LEE, D. & KIM, Y. (2021) Mathematical model of stat signalling pathways in cancer development and optimal control approaches. *R. Soc. Open Sci.*, **8**, 210594.

LIMA, EABF, ODEN, JT, HORMUTH, DA, YANKEELOV, TE & ALMEIDA RC (2016) Selection, calibration, and validation of models of tumor growth. *Math. Models Methods Appl. Sci.*, **26**, 2341–2368.

MARSZALEK-GRABSKA, M., WALCZAK, K., GAWEL, K., WICHA-KOMSTA, K., WNOROWSKA, S., WNOROWSKI, A. & TURSKI, W. A. (2021) Kynurenine emerges from the shadows—current knowledge on its fate and function. *Pharmacol. Ther.*, **225**, 107845.

MATLAB (2010) *Version 7.10.0 (R2010a)*. Natick, Massachusetts: The MathWorks Inc.

NAVE, O. & SIGRON, M. (2022) A mathematical model for the treatment of melanoma with the braf/mek inhibitor and anti-pd-1. *Appl. Sci.*, **12**, 12474.

ORIMO, A., GUPTA, P. B., SGROI, D. C., ARENZANA-SEISDEDOS, F., DELAUNAY, T., NAEEM, R., CAREY, V. J., RICHARDSON, A. L. & WEINBERG, R. A. (2005) Stromal fibroblasts present in invasive human breast carcinomas promote tumor growth and angiogenesis through elevated sdf-1/cxcl12 secretion. *Cell*, **121**, 335–348.

PORVASNIK, S., SAKAMOTO, N., KUSMARTSEV, S., ERUSLANOV, E., KIM, W.-J., CAO, W., URBANEK, C., WONG, D., GOODISON, S. & ROSSER, C. J. (2009) Effects of cxcr4 antagonist ctce-9908 on prostate tumor growth. *Prostate*, **69**, 1460–1469.

RUIZ-MARTINEZ, A., GONG, C., WANG, H., SOVE, R. J., MI, H., KIMKO, H. & POPEL, A. S. (2022) Simulations of tumor growth and response to immunotherapy by coupling a spatial agentbased model with a whole-patient quantitative systems pharmacology model. *PLOS Comput. Biol.*, **18**, 1–32.

SUNG, H., FERLAY, J., SIEGEL, R. L., LAVERSANNE, M., SOERJOMATARAM, I., JEMAL, A. & BRAY, F. (2021) Global cancer statistics 2020: Globocan estimates of incidence and mortality worldwide for 36 cancers in 185 countries. *CA Cancer J. Clin.*, **71**, 209–249.

TABOR, M. (1988) *Chaos and Integrability in Nonlinear Dynamics: An Introduction*. Wiley.

VERHULST, F. (2010) *Methods and Applications of Singular Perturbations*. Springer.

WALCZAK, K., LANGNER, E., MAKUCH-KOCKA, A., SZELEST, M., SZALAST, K., MARCINIAK, S. & PLECH, T. (2020) Effect of tryptophan-derived ahr ligands, kynurenine, kynurenic acid and ficz, on proliferation, cell cycle regulation and cell death of melanoma cells—in vitro studies. *Int. J. Mol. Sci.*, **21**, 7946.

WALTER, W. (1998) *Ordinary Differential Equations*. Springer.

WIGGINS, S. (2003) *Introduction to Applied Nonlinear Dynamical Systems and Chaos*. Springer.

WONG, D. & KORZ, W. (2008) Translating an antagonist of chemokine receptor cxcr4: from bench to bedside. *Clin. Cancer Res.*, **14**, 7975–7980.

## Appendix

Before we present the proof of Theorem 1, we recall the Bendixon–Dulac criterion (e.g. Layek, 2015) concerning the non-existence of a periodic solution for a planar system. For a planar system $\dot{x} = f(x, y)$ and $\dot{y} = g(x, y)$ with a vector field $F = (f, g)$, if $div(F) = \partial f/\partial x + \partial g/\partial y \neq 0$ on a simply connected subset $\Omega$ of $\mathbf{R}^2$ (a region in the plane without gaps/holes), then there is no non-constant periodic solution in $\Omega$.

## Proof of Theorem 1

**Proof of (i).** The equilibria of (9)–(10) are solutions of the simultaneous equations

$$k_1(R_0 - P - Q)(L_0 - P) = k_{-1}P, \tag{A.1}$$

$$k_2(R_0 - P - Q)(X_0 - Q) = k_{-2}Q. \tag{A.2}$$

Dividing the left-hand sides and the right-hand sides of the equations (A.1) and (A.2) yields

$$\frac{k_1(L_0 - P)}{k_2(X_0 - Q)} = \frac{k_{-1}P}{k_{-2}Q}. \tag{A.3}$$

Solving for $Q$, we obtain

$$Q = \frac{X_0 P}{P + \frac{k_1 k_{-2}}{k_2 k_{-1}}(L_0 - P)}. \tag{A.4}$$

Expressing $Q$ from equation (A1), we obtain

$$Q = R_0 - P - \frac{k_{-1}P}{k_1(L_0 - P)}. \tag{A.5}$$

The systems (A.1)–(A.2) are equivalent to the systems of equations (A.4)–(A.5), where each equation gives $Q$ as a function of $P$. Equation (A.4) defines a continuous increasing function of $P$ on the interval $[0, L_0]$. Considered on the interval $[0, L_0]$, its graph connects the points $(0, 0)$ and $(L_0, X_0)$. The function of $P$ given in (A.5) is continuous and decreasing on the interval $[0, L_0]$ from $R_0$ to $-\infty$. Then we can conclude that the graphs of the function in (A.4) and (A.5) intersect exactly once at a point $(P^*, Q^*)$, which satisfies $0 < P^* < L_0$ and $0 < Q^* < X_0$. It follows from (A.5) that $P^* + Q^* < R_0$. Therefore, $(P^*, Q^*)$ is a unique solution of (A.1)–(A.2) in $\Omega$ or, equivalently, a unique equilibrium of (9)–(10) in $\Omega$.

**Proof of (ii).** The Jacobian $J$ of the vector field $F$ of the system (9)–(10) can be written as

$$J = \begin{pmatrix} k_1(\alpha + \beta) - k_{-1} & k_1\beta \\ k_2\gamma & k_2(\alpha + \gamma) - k_{-2} \end{pmatrix},$$

where $\alpha := P + Q - R_0$, $\beta := P - L_0$ and $\gamma := Q - X_0$. Observe $\alpha, \beta, \gamma < 0$ when $(P, Q)$ is contained in the interior of $\Omega$.

We do not evaluate the point $(P^*, Q^*)$ to avoid dealing with tedious expressions. We prove that it is a hyperbolic sink by showing that the eigenvalues $\lambda_1$ and $\lambda_2$ of the Jacobian evaluated at $(P^*, Q^*)$ lie to the left of the imaginary axis in the complex plane. To this end, it is sufficient to show that $\lambda_1\lambda_2 = \det(J)_{|(P^*, Q^*)}$ is positive, while $\lambda_1 + \lambda_2 = \text{trace}(J)_{|(P^*, Q^*)}$ is negative. The determinant of $J$, $\det(J)$ simplifies to

$$\begin{aligned}
\det(J) &= k_1 k_2(\alpha + \beta)(\alpha + \gamma) - k_1 k_{-2}(\alpha + \beta) - k_{-1}k_2(\alpha + \gamma) + k_1 k_2\beta\gamma + k_{-1}k_{-2} \\
&= k_1 k_2\Big((\alpha + \beta)(\alpha + \gamma) - \beta\gamma)\Big) - k_1 k_{-2}(\alpha + \beta) - k_{-1}k_2(\alpha + \gamma) + k_{-1}k_{-2} \\
&= k_1 k_2\alpha(\alpha + \beta + \gamma) - k_1 k_{-2}(\alpha + \beta) - k_{-1}k_2(\alpha + \gamma) + k_{-1}k_{-2}.
\end{aligned}$$

Since $\alpha, \beta, \gamma < 0$ in the interior of $\Omega$, $(P^*, Q^*)D$, the terms $k_1 k_2\alpha(\alpha + \beta + \gamma)$, $-k_1 k_{-2}(\alpha + \beta)$ and $-k_{-1}k_2(\alpha + \gamma)$ are both positive, and thus $\det(J) > 0$.

Next, in the same vein, we have $\text{trace}(J) = \text{div}(F) = (k_1(\alpha + \beta) - k_{-1}) + k_2(\alpha + \gamma) - k_{-2}) < 0$ in the interior of $D$. Thus, $(P^*, Q^*)$ is a hyperbolic sink, and hence a locally asymptotically stable equilibrium. Further, the product of the non-diagonal entries of $J$ is positive, which implies that the eigenvalues of $J$ are real and distinct. Hence, the equilibrium is a stable proper node.

**Proof of (iii).** The set $\Omega$ is determined in (11) by five linear inequalities. Hence, it is always a convex polygon. In a typical case when $R_0 < L_0$ and $R_0 < X_0$, the set $\Omega$ is a triangle. However, if the stated inequalities do not hold, $\Omega$ can be a rectangle, a trapeze or a pentagon. We prove that $\Omega$ is positively invariant set for the dynamical system (9)–(10) by using the so-called tangent condition (Walter, 1998, Section 10.XV), namely that at every point of the boundary $\partial\Omega$ the dot product of the vector field and any outer normal vector at that point is non-positive. Let us recall that a vector $v(x) \neq 0$ is called outer normal vector to $\Omega$ at $x \in \partial\Omega$ if the open ball with center $x + v(x)$ and radius $|v(x)|$ has no intersection with $\Omega$. This definition is applicable not only to the sides of the polygon $\Omega$, but also at the vertices. The boundary consists of all points satisfying the five inequalities in (11), while at least one of them is satisfied as an equality. Verifying the tangent condition entails substituting in the right-hand side of

(9)–(10) the respective values of $P$ and/or $Q$ and calculating the dot product with the outer normal. As illustration, consider the line segment $P + Q = R_0$. Its outer normal vector is $(1, 1)$. On this segment, we have $\frac{dP}{dt} = -k_{-1}P$ and $\frac{dQ}{dt} = -k_{-2}Q$. Therefore for the said dot product, we have $-k_{-1}P - k_{-2}Q \leq 0$. Similarly, one considers the rest of the boundary to establish that the tangent condition holds. Hence, $\Omega$ is positively invariant.

**Proof of (iv).** Suppose there exists a point $z \in \Omega$ that is not contained in the basin of attraction of the sink $(P^*, Q^*)$. This implies that the $\omega$-limit set of the trajectory passing through $z$ is contained in $\Omega$ by (iii). Owing to a result of a Poincare and Bendixon (e.g. Dumortier *et al.*, 2006), for a planar flow, the $\omega$-limit set would either be an equilibrium solution or a periodic solution or a saddle-loop. Since $div(F) < 0$ on $\Omega$, a periodic solution is ruled out by Bendixon–Dulac criterion, and since $(P^*, Q^*)$ is the unique equilibrium that is a sink, a saddle loop is also not possible. Thus, no such $z$ exists, and hence $\Omega$ is contained within the basin of the $(P^*, Q^*)$. ■